

## ARTICLE OPEN



# Degradation mechanism analysis of $\text{LiNi}_{0.5}\text{Co}_{0.2}\text{Mn}_{0.3}\text{O}_2$ single crystal cathode materials through machine learning

Wuxin Sha<sup>1,2,6</sup>, Yaqing Guo<sup>2,3,6</sup>, Danpeng Cheng<sup>2</sup>, Qigao Han<sup>3</sup>, Ping Lou<sup>4</sup>, Minyuan Guan<sup>1,5</sup>, Shun Tang<sup>2</sup>, Xinfang Zhang<sup>1</sup>, Songfeng Lu<sup>5</sup>, Shijie Cheng<sup>2</sup> and Yuan-Cheng Cao<sup>1,2</sup>✉

$\text{LiNi}_{0.5}\text{Co}_{0.2}\text{Mn}_{0.3}\text{O}_2$  (NCM523) has become one of the most popular cathode materials for current lithium-ion batteries due to its high-energy density and cost performance. However, the rapid capacity fading of NCM severely hinders its development and applications. Here, the single crystal NCM523 materials under different degradation states are characterized using scanning transmission electron microscopy (STEM). Then we developed a neural network model with a two-sequential attention block to recognize the crystal structure and locate defects in STEM images. The number of point defects in NCM523 is observed to experience a trend of increasing first and then decreasing in the degradation process. The space between the transition metal columns shrinks obviously, inducing dramatic capacity decay. This analysis sheds light on the defect evolution and chemical transformation correlated with layered material degradation. It also provides interesting hints for researchers to regenerate the electrochemical capacity and design better battery materials with longer life.

npj Computational Materials (2022)8:223; <https://doi.org/10.1038/s41524-022-00905-5>

## INTRODUCTION

$\text{LiNi}_x\text{Co}_y\text{Mn}_{1-x-y}\text{O}_2$  (NCM) has become one of the most popular cathode materials for current lithium-ion batteries due to its high capacity and cost-effectiveness. However, the rapid capacity fade over cycles of NCM severely hinders its development and applications. The advanced electron microscopy investigations on the degradation mechanisms of NCM play indispensable roles in the design of high-energy-density lithium-ion battery materials. Current electron microscopy allows the direct visual recognition of atom-level configuration information from the host crystal structure, lattice plane distortion to even single point defect, providing rich information of battery material processes and properties. Consequently, many researchers have investigated the origin of the degradation mechanism in NCM through advanced electron microscopy. Structural defects such as Li/transition metal atom mixing or oxygen vacancies will cause further phase transitions, surface reconfiguration, and accompanied by the evolution of oxygen<sup>1,2</sup>. In addition, the electrolyte solvent with a narrow electrochemical stability window will react with  $\text{Ni}^{4+}$ , leading to the oxidative decomposition of the electrolyte<sup>3</sup>. Furthermore, interfacial side reactions and dissolution of transition metals lead to the degradation of performance. Meanwhile, volume changes during cycling and the generation of microcracks during cycling, and the generation of thicker cathode electrolyte interface (CEI) films on the surface are the main causes of cathode material degradation<sup>4,5</sup>. These common degradation phenomena of NCM cathodes are summarized in Fig. 1.

Although the amount of high spatial/temporal resolution cathode material data is increasing, the degradation dynamic information inferred from advanced characterization methods is very limited. Because the interpretation of microscopy data heavily relies on the 'intuition' of experienced researchers and

many profound degradation features often remain unexploited. The inherent limitations of manual analysis in volume and speed hinder the deep utilization of advanced characterizations<sup>6</sup>. Therefore, it is urgent to develop an automatic framework for material characterization image processing, which can efficiently locate and track atom defects, or other microstructure configurations, and quantitatively study the property evolutions in materials. Artificial intelligence (AI) is good at big data processing and knowledge mining because of its flexible algorithm framework and powerful hardware foundation, which brings more opportunities for the development of material science.

Fortunately, some tentative studies have made admirable progress in the field of AI-assisted electron microscopy. Lee et al. proposed a genetic algorithm (GA) image processing technique that enables the analysis of over 150,000 nanoparticles with a high precision of 99.75%. This technique provides an example for further data mining in the field of transmission electron microscopy (TEM)<sup>7</sup>. Han et al. built an encoder-decoder semantic segmentation network called 2D material optical identification neural network (2DMOINet)<sup>8</sup>. This architecture is configured for pixel-wise material identification of microscopy images in real-time and for finding correlations between the microscopy images and material physical properties. Similar advances are also achieved in locating morphology features from scanning electron microscopy (SEM) data, tracking phase evolution in scanning transmission electron microscopy (STEM) data, and quantifying the protein dynamics in atomic force microscopy (AFM) data<sup>9–11</sup>.

Nevertheless, there are still few AI frameworks designed for battery material analysis. In this paper, a deep learning u-net network, one of the common AI algorithm frameworks, is improved to study the capacity degradation mechanism of

<sup>1</sup>School of Computer Science and Technology, Huazhong University of Science and Technology, Wuhan 430074, China. <sup>2</sup>State Key Laboratory of Advanced Electromagnetic Engineering and Technology, School of Electrical and Electronic Engineering, Huazhong University of Science and Technology, Wuhan 430074, China. <sup>3</sup>Wuhan National Laboratory for Optoelectronics, Huazhong University of Science and Technology, Wuhan 430074, China. <sup>4</sup>State Grid Huzhou Electric Power Supply Company, Huzhou 313000, China. <sup>5</sup>School of Cyber Science & Engineering, Huazhong University of Science and Technology, Wuhan 430074, China. <sup>6</sup>These authors contributed equally: Wuxin Sha, Yaqing Guo. ✉email: yccao@hust.edu.cn

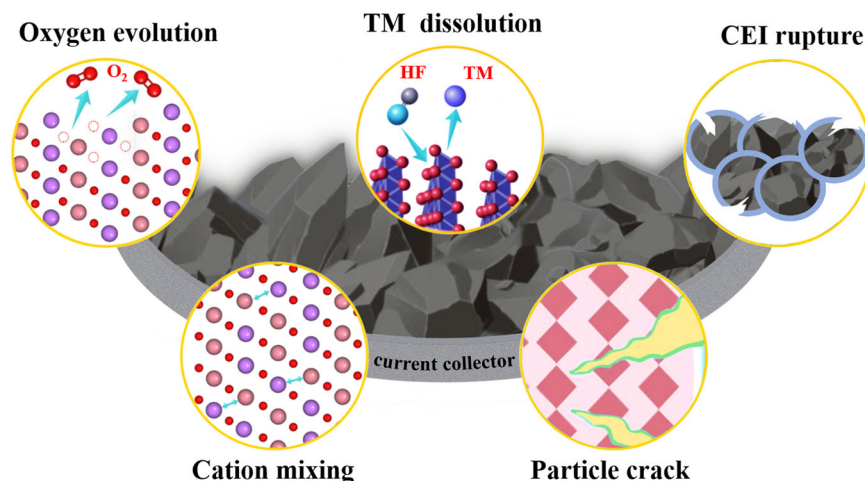


**Fig. 1 Schematic diagrams describing degradation phenomena of NCM cathodes.** The whole picture background is based on the microscopic profile of cathode particles on the current collector. The five magnified cycles represent some common cathode material degradation mechanisms, such as the evolution of oxygen, the dissolution of transition metals (TM), the rupture of CEI films, the cation mixing and the generation of particle cracks.

ternary cathode materials. Firstly, a neural network model is established to process the STEM images to identify the host crystal structure and locate the defects in a few seconds. Meanwhile, these defects are classified by a two-sequential attention module, and three main defects are found: transition metal vacancies, lithium vacancies, and interstitial atoms. These point defects in single crystal NCM523 are researched under different degradation states, including the layered, spinel, and rock-salt structures. It is concluded that the number of overall point defects in NCM523 experiences a trend of increasing first and then decreasing in the whole degradation process. Combined with the analysis of electron energy loss spectroscopy (EELS) and electrochemistry characterization, it is found that defect evolution is correlated with the increase of battery impedance and capacity fading. Finally, the major lattice parameters in NCM523 materials are analyzed quantitatively. The space between the transition metal dense layers shrinks from 4.86 Å to 1.96 Å, which means the decreasing number of crystal sites to accommodate lithium ions, inducing capacity decay. These machine-learning statistic results provide effective insights for battery material design.

This research consists of sample preparation of ternary materials, electrochemical and electron microscopy characterization, and machine learning. The complete machine learning paradigm includes three modules: algorithm structure building, dataset generation, and model training. The experimental details are described in the following parts.

## RESULTS AND DISCUSSION

### Neural network architecture

We keep the basic architecture of skip connections between completely symmetrical encoder-decoder structures in U-net<sup>12</sup>, due to its essential fusion with the fine and coarse-grained information, as shown in Fig. 2. Compared with the original one, the contributions of this network are summarized in three operations. Firstly, for each encoder and decoder, a two-sequential attention block is introduced to give an eye to salient parts of images. More details about attention are discussed in the next paragraph. Secondly, simple concatenation skip links are replaced by residual connections to get rid of redundant information. Because shallow layer information may not concatenate well with deep-layer information, which will lead to redundancy or even worse result. Residual connections could decrease the channel number of the feature map by adding

operations, thus reducing computational complexity. Hence the deeper network could also have satisfying training and detecting performance even when the shallow layer feature map has a bad influence on the deeper one. Thirdly, batch normalization operation converts the inputs into a normal distribution with a mean of 0 and a standard deviation of 1 for training acceleration.

To help the model select focus on salient parts from tremendous pixels in an electron micrograph, we proposed a two-sequential attention block inserting network with a residual connection as presented in Fig. 3. The overall operation is summarized as:

$$\mathbf{F} = \mathbf{F}_c(\mathbf{F}) \otimes \mathbf{F} \quad (1)$$

$$\mathbf{F}_{\text{out}} = \mathbf{F}_s(\mathbf{F}) \otimes \mathbf{F} \quad (2)$$

Where  $\mathbf{F}$  is the input feature map,  $\mathbf{F}_c$  infers channel attention,  $\mathbf{F}_s$  denotes spatial attention, and  $\otimes$  represents element-wise multiplication. Channel attention multiplies different weights to each channel of a feature map, thus focusing on meaningful features given an input image. Inspired by Wang et al.'s work<sup>13</sup>, we use an Efficient Channel Attention model as consideration of interaction among every channel and its  $k$  neighbors. An average pooling is first applied to the feature map, and 1D convolution of size  $K$  is followed, where  $K$  is calculated in the following Equation. Besides, the output of convolution is fed to a sigmoid function.

$$K = \left\lfloor \frac{\log_2(C)}{\gamma} + \frac{b}{\gamma} \right\rfloor \text{odd} \quad (3)$$

Where  $C$  is channel dimension,  $\gamma$  and  $b$  are parameters of mapping function ( $\gamma = 2$  and  $b = 1$  are used in the experiment).

Spatial Attention cares locations of target objects. We concatenate both max pooling and average pooling of feature maps to capture attention along the channel axis. To aggregate information, the result is then forwarded to a standard convolution layer, forming a final attention map.

### Generation of training data

Generating training data for neural networks is an important challenge in this study. It is unpractical to collect real STEM experimental images as training data. On the one hand, the electron microscopy experiment is expensive, and the crystal structure and defect types that can be collected by a single laboratory are extremely limited. On the other hand, it is time-consuming and inaccurate to label all atom positions manually.

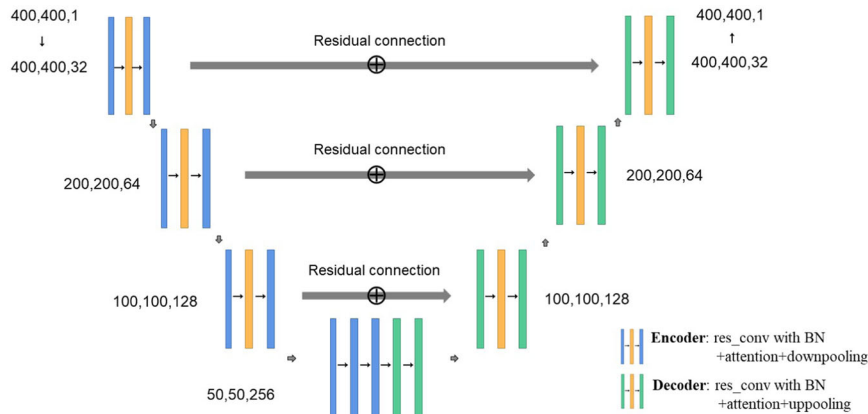


**Fig. 2** The architecture of attention U-net. The symbol 'res\_conv' means residual connections and convolution operation. BN means batch normalization operation.

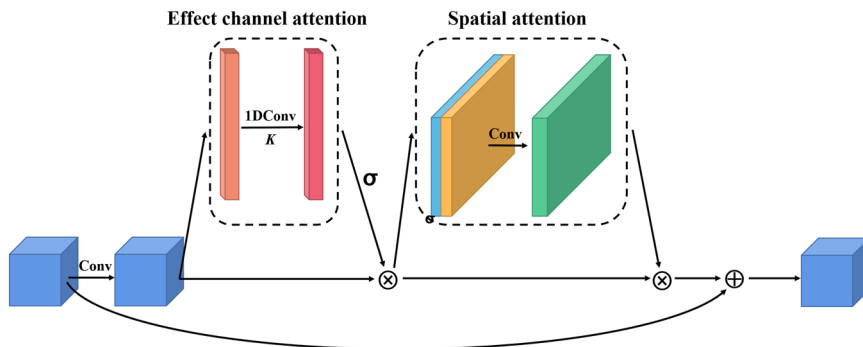


**Fig. 3** The flowchart of a two-sequential attention block with a residual connection. Conv means convolution operation. 1DConv and  $K$  mean 1D convolution with kernel size  $K$ .  $\sigma$  means sigmoid activation function. A straight line or curve with an arrow represents the data transfer.  $\otimes$  represents element-wise multiplication.  $\oplus$  represents residual connection.

Therefore, simulated methods are applied to build the training datasets as shown in Fig. 4. Firstly, the atomic simulation environment, a Python library for working with atoms, is employed to generate a large number of atomic cluster models, including layered, spinel, and rock-salt structures. The space groups for layered, spinel and rock-salt structures are  $R\bar{3}m$  ( $a = 2.877 \text{ \AA}$ ,  $b = 14.228 \text{ \AA}$ ),  $Fd\bar{3}m$  ( $a = 8.219 \text{ \AA}$ ) and  $Fm\bar{3}m$  ( $a = 4.177 \text{ \AA}$ ), respectively<sup>14</sup>.

Considering the serious loss of lithium and transition metal Mn and Co and the existence of rock-salt phase structure during NCM degradation, it is reasonable to replace degraded NCM with NiO which is also rock-salt structure<sup>15</sup>. Similarly, in order to simplify the atomic configuration, lithium cobalt oxide ( $\text{LiCoO}_2$ , LCO) and lithium manganate ( $\text{LiMn}_2\text{O}_4$ , LMO) are used to generate layered structure models and spinel structure models, respectively<sup>16–18</sup>. The STEM images of LCO, LMO, and NiO are basically consistent with the crystal structure evolution of NCM523 during aging.

Transition metal vacancies, lithium vacancies, interstitial atoms, and other point defects are introduced into the primary crystals of these atomic models. After introducing defects, the necessary geometry optimization of atom clusters is carried out by using the BFGS optimization method and GPAW potential calculator built in ASE (atomic simulation environment, a Python library)<sup>19</sup>. The convergence conditions such as maximum forces are set to a larger value to reduce the calculation time and maintain the salient lattice distortion caused by defects. Because neural networks need the visual effect of lattice distortion, rather than precisely calculating the total system energy by the atom positions. The model diagrams before and after local geometry optimization are shown in Fig. 4a. The trace of geometry

optimization is clearly visible for the 3~5 atoms near the point defect center location.

Then the simulated electron microscope images for different atomic clusters are generated using a multislice algorithm<sup>20,21</sup>. In this method, the electron beam is assumed to be a plane wave, and the incident wave function of the electron beam is determined according to the preset electron microscope parameters, such as spherical aberration coefficient, electron dose, annular incident angle, etc., and then incident on the surface of the atomic cluster. The state of the exit wave function at different positions is changed according to the interaction of the electronic structures of each atom. Then the plane projection of the exit wave function is calculated. The intensity value of the projection is used as the pixel value to generate a simulated image according to the contrast transfer function. The simulated STEM images are shown in Fig. 4b. The real defect coordinates used in atomic cluster models are used as the training label. Such a labeling method is more accurate and efficient than 'by hand' manually. The full dataset is available at Zenodo<sup>22</sup>. Three images from this dataset were previously analyzed by some of the authors in the context of Regeneration<sup>23</sup>.

### Training process

The whole process for machine learning-based image analysis is shown in Fig. 5. As the first step of this analysis, the designed attention neural network is encapsulated into a python file for the later main program call to realize the end-to-end semantic segmentation of STEM images. The input of the network is the simulated STEM images of different atom models. The output of the network is the location of the point defect in the atomic cluster.

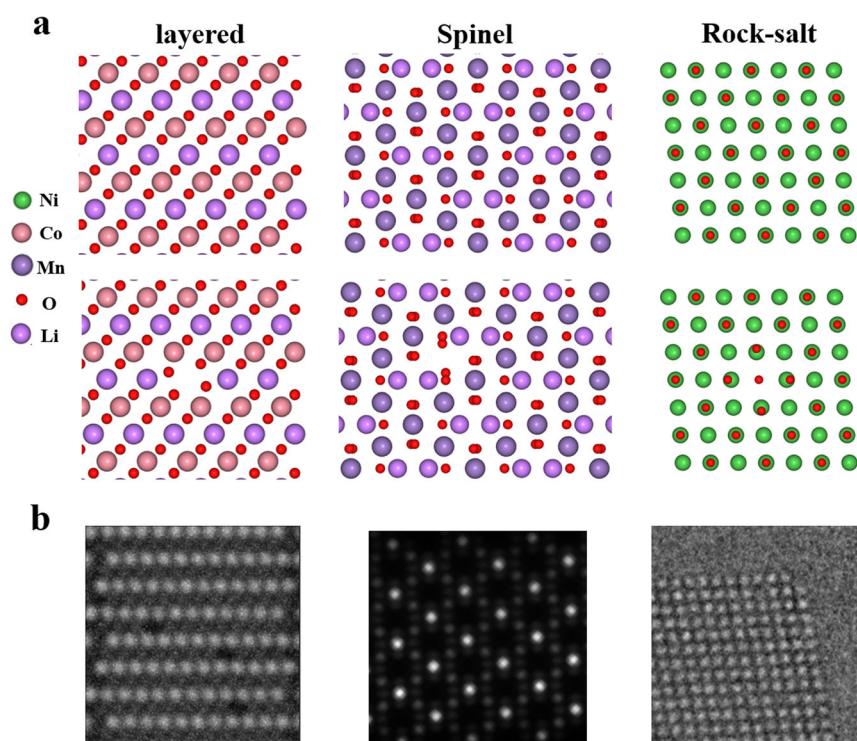


**Fig. 4 Procedure for generating training data.** **a** The original and geometry-optimized atom models for layered, spinel, and rock-salt structures. **b** The simulated STEM images for layered, spinel, and rock-salt structures.

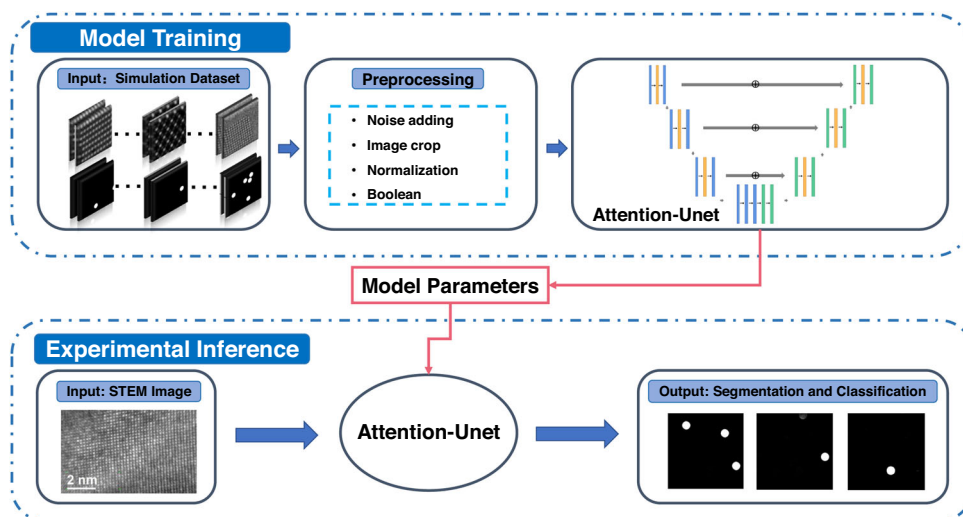


**Fig. 5 The whole framework of model training and STEM image inference.** During the model training stage, the simulation STEM images and the corresponding labels compose a paired dataset. After dataset preprocessing and training, the designed attention neural network realizes semantic segmentation. During the experimental image inference stage, the model parameters at the end of training are retained in the model for defect detection of real STEM images.

After the above data generation step, the simulated STEM images and the corresponding labels have formed a paired dataset. Then images and labels with different crystal structures are cut to a uniform size (pixel value  $400 \times 400$ ). Three different crystal structures are randomly mixed to form an effective dataset containing 3000 pairs of input and output. The pixel values of input images are normalized to increase the training efficiency. The labels are converted to Booleans to facilitate the employment of loss function in the later stage. The batch size is designed as 5 and the epoch number is set as 20. The network python file is called to start the training process. During this period, the network

parameters are continuously adjusted by random gradient descent algorithm. Finally, the model parameters at the end of training are retained for defect detection of real STEM images.

#### Loss function design

The U-net is trained using mean-squared error and L2 regularization technique as loss function. The formulation is

$$L = \sum_n \|\mathbf{P}_n - \mathbf{p}_n\|^2 + \frac{1}{2} \lambda \sum_i \mathbf{W}_i^2 \quad (4)$$

where  $L$  represents the loss value that needs to be minimized during the training process.  $\mathbf{P}$  is the output and  $\mathbf{P}$  is the ground truth. The size of the weights is regularized with a penalty term  $\lambda$ . The generalization ability of the model is guaranteed by the large variability of the training datasets. However, the model parameters fall into a local optimal state in the training process. The number of point defects in STEM pictures is far less than the number of atoms, the picture labels are sparse. If only MSE and L2 regularization are used as the loss function, the parameter distribution of the whole model is easy to fall into local optimization. Because when all the output values of the model approach 0, the values of MSE and L2 regularization are very small, almost in the state of gradient disappearance. In order to solve this problem, we enlarged the label pixel size of point defects in

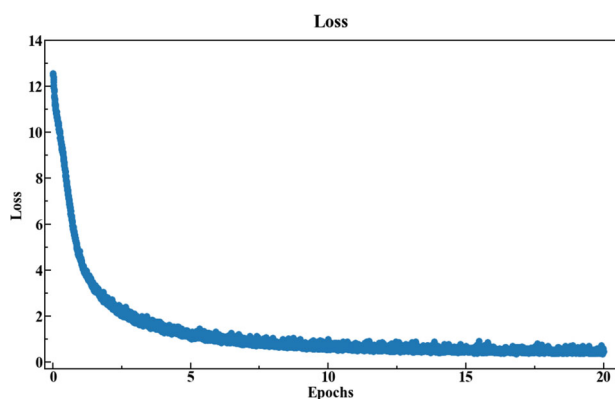


**Fig. 6** The decreasing process of loss value on simulated STEM images during the training stage. Epoch defines the number of times the learning algorithm works in the entire training dataset. Here it is set to 20. The loss value measures the difference between the network output images and the labeled images.

the early training stages. Through comparative tests and ablation experiments, it was found that the effect of this loss function was improved. As can be seen from Fig. 6, training loss drops sharply and then tends to converge, which is a typical result of successful neural network training. Finally, loss remained with small fluctuations between different batches during the training of epoch 20. Therefore, the training is stopped after 20 epochs. The model parameters are saved and applied for real STEM defect detection.

### Electrochemical and microscopic characterizations

We carried out a series of electrochemical and microscopic characterizations to explore the aging mechanism in NCM single-crystal particles. As shown in Fig. 7a, there remains a pair of inconspicuous redox peaks in the cyclic voltammetry (CV) curve, and the CV curve with lower currents and larger peak shifts compared to Fig. 7b (the CV curve of commercial NCM523). It indicates that the degraded material has poorer redox performance and lower capacity than that of commercial NCM523. This can be confirmed by the rate performance of degraded NCM and commercial NCM523 (Fig. 7c). The commercial NCM523 exhibits a high rate performance of  $170.8 \text{ mAh g}^{-1}$  at 1 C and  $121.1 \text{ mAh g}^{-1}$  at 5 C, while the degraded NCM523 shows only  $4.6 \text{ mAh g}^{-1}$  at 0.1 C.

Cathode failure is mainly related to the crystal structure of the material, while a thick CEI film on the surface of the degraded material hinders ion diffusion, and phase transformations near the surface of the material as well as inside the material lead to the degradation of the material properties. Hence, the high-resolution X-ray photoelectron spectroscopy (XPS) measurement was applied to finely characterize the composition of the CEI film. As shown in Fig. 8, the peak at 284.8 eV is associated with C-C/C-H, the peaks at 286.9 eV (C-O) and 288.0 eV (C=O) mainly come from the  $\text{Li}_2\text{CO}_3$  phase in the CEI, and the peak at 290.4 eV peak corresponds to polyvinyl difluoride (PVDF) or the  $\text{ROCO}_2\text{Li}$  salt<sup>24</sup>. In addition,

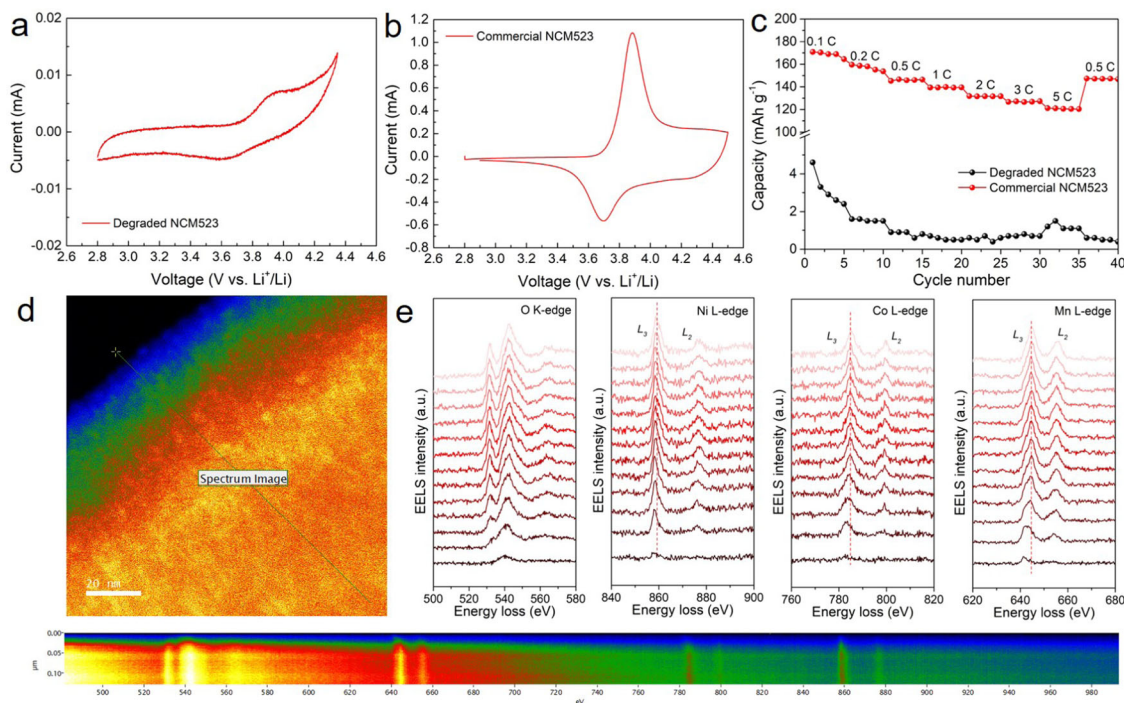


**Fig. 7** Electrochemical characterizations of NCM523. **a** The CV curves of degraded NCM523 with the scan rate of  $0.1 \text{ mV s}^{-1}$ . **b** The CV curves of commercial NCM523 with the same scan rate. **c** The rate performance of degraded NCM523 and commercial NCM523. **d** High-resolution HAADF STEM image. **e** The comparison of EELS low-loss spectra between the surface and the interior.

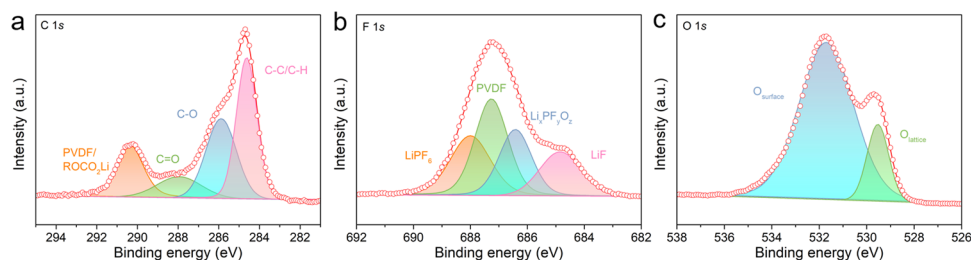


**Fig. 8** XPS spectra characterization for NCM523 powders. **a–c** Show the high-resolution XPS spectra of the C 1s, F 1s, and O 1s for degraded NCM523.

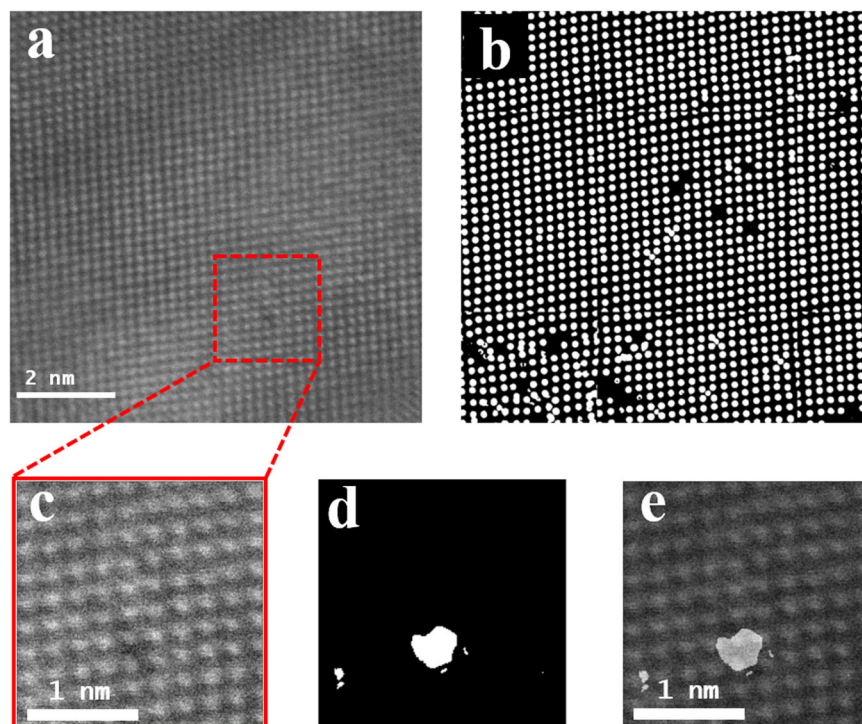


**Fig. 9** Typical inference results of attention U-net. **a** Original STEM image for rock-salt phases in NMC523. The scale bar represents 2 nm. **b** Positions of transition metal atoms located by Attention U-net. **c** An enlarged detail part of **a** as an input to the attention U-net. The scale bar represents 1 nm. **d** The network output result corresponding to point defects in **c**. **e** The superposition of **c** and **d** showing the defect locating effect of attention U-net. Error bars represent one standard deviation computed across different STEM images. The scale bar represents 1 nm.

the F 1s spectra of degraded NCM523 can be divided into four peaks corresponding to  $\text{LiPF}_6$  (688.1 eV), PVDF (687.3 eV),  $\text{Li}_x\text{PF}_y\text{O}_z$  (686.4 eV), and LiF (684.8 eV), indicating the existence of LiF and organic components in the CEI. Furthermore, in the O 1s core region, the  $\text{O}_{\text{surface}}$  mostly comes from the organic components,  $\text{Li}_2\text{CO}_3$  and adsorbed components. While the  $\text{O}_{\text{lattice}}$  corresponds to the NMC lattice oxygen peak, which is always distinguished in the NCM materials<sup>23</sup>.

Furthermore, EELS was used to further investigate the chemical valence information of atoms in cathode particles. The EELS signal is scanned from the area indicated by the arrow (Fig. 7d), corresponding to the thin surface and thick center area of NCM particles. In addition, the overall signal variation of the EELS with a slight signal shift from the surface to the inner ~130 nm is shown at the bottom of Fig. 7. The EELS lines with 10 nm acquisition of one signal spectrum scheme scan are shown in Fig. 7e. The K-edge of O originates from O 1s excitation to unoccupied 2p orbitals above the Fermi level. The O K-edge is related to the hybridization between the O 2p and C 2p states, which is mainly influenced by the CEI composition of the material surface. While the interior is associated with the hybridization of 3d and 4sp orbitals of transition metal atoms, leading to the splitting of the peaks<sup>25</sup>. In

addition, the low-loss spectrum of Ni L-edge, Co L-edge, and Mn L-edge show a blue shift of absolute energy from the surface thin region to the central thick region, indicating that the oxidation state of transition metal atoms on the surface is low due to the surface oxygen loss during the cycle.

These characterization data contain rich degradation features. However, it is inefficient to mine millions of atoms' structural information by researchers' experience alone. Hence, we have developed a deep learning framework to efficiently locate and track atom clusters, single atoms, or lattice defects, and quantitatively study the phase reactions in materials. The following parts are the research details.

### Deep learning-based characterization data mining

The proposed u-net model is employed to locate the atomic defects in the NCM STEM experimental images. All inference results for experimental STEM images were evaluated using the naked eye as an external judgment. Although our model only uses simulated STEM images for training, it can accurately identify the point defects in experimental STEM images as shown in Fig. 9.

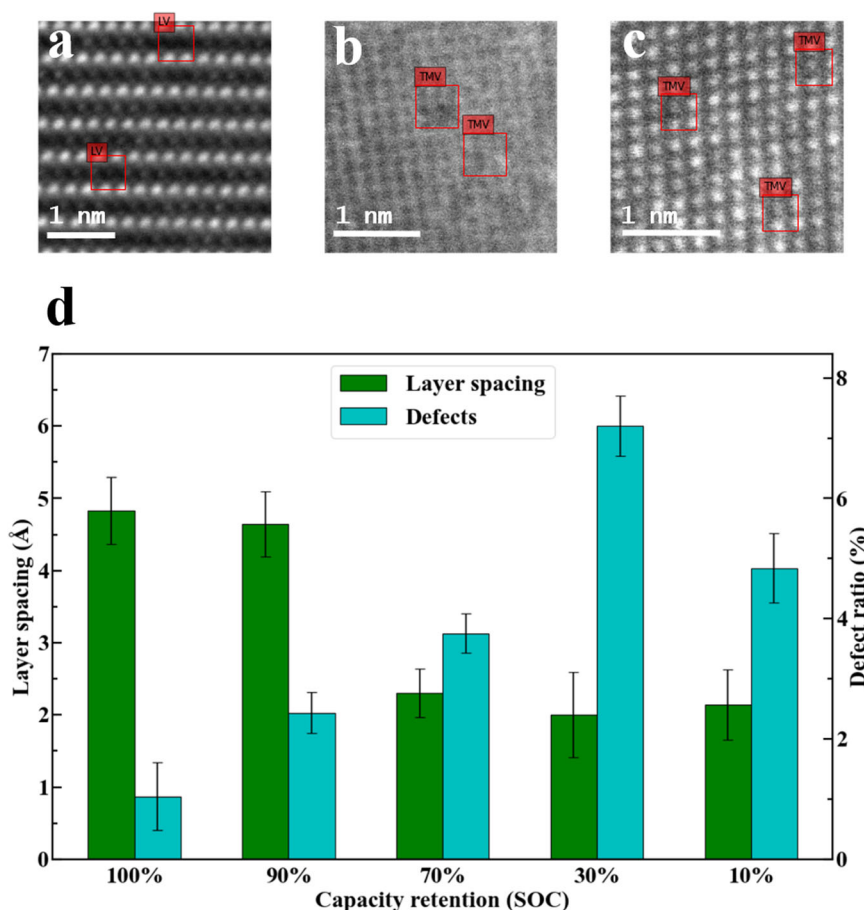


**Fig. 10** The quantitative analysis results of NCM523 degradation. **a–c** are the point defect inference results for layered, spinel, and rock-salt phases in NCM523, respectively. The embedded markups are LV (Lithium vacancy) and TMV (transition metal vacancy). The scale bars in **a–c** all represent 1 nm. **d** TM layer spacings and point defect ratios in NCM523 STEM images with different SOC. Green bars represent layer spacing and cyan bars represent point defect ratio. Error bars represent one standard deviation computed across different STEM images.

NCM523 mainly contains three kinds of elements: transition metal (TM) elements, oxygen elements, and lithium elements. Unfortunately, oxygen atoms are basically invisible in HAADF images because of the atomic number contrast. Based on the understanding of point defect distribution, transition metal vacancy, Li vacancy, and interstitial atom are determined to be labeled and quantitatively analyzed. Lithium vacancies are often observed in the layered phase (Fig. 10a) and transition metal vacancies and interstitial atoms often exist in the form of composite defects together (Fig. 10c). Interstitial atoms refer to individual atoms outside of the normal crystal sites.

After the training of several epochs, the network correctly identifies the location of different point defects. A segmentation of the background map into several distinct object classes corresponding to vacancies or interstitial atoms. A classic transition metal vacancy in rock-salt structure image is taken as an example. As shown in Fig. 9c, the lack of transition metal atom in this specific crystal site leads to the distortion of several adjacent atoms. Therefore, the periodicity of pixel value distribution is destroyed near the vacancy region. The network can basically judge the defects by the degree of periodicity damage and the difference between pixel values. The model probably learned that atoms with darker gray values are likely to be vacancies. Hence, most atoms are correctly assigned to their classes. The last layer of the network applies the sigmoid activation function, so the output pixel values range from 0 to 1. Higher output pixel values represent a larger defect probability (Fig. 9d). It may be more intuitive to superimpose the output probability value on the input image as shown in Fig. 9e.

We also performed the confusion matrix experiment using the simulated dataset, as shown in Table 1. Three kinds of defects, Li vacancy, TM vacancy, and TM interstitial, have been quantitatively analyzed, and lattice atom and background are also counted in the table. The number 0 in the lower right corner of the table indicates that there are no atoms in the background of STEM images. It can be seen from the table that there is no confusion between different defects and atomic categories. Because each category will have a separate channel for output in the network. The misclassification error of the network mainly comes from the confusion between background and atom defects, which is shown by the numbers in the last row and the numbers in the last column.

Then, we calculate the overall performance of the network with four different metrics: Precision, Recall,  $F_1$  score and IOU. Their calculation formula is shown in Supplementary Note 3.  $F_1$  score is the harmonic average of precision and recall. IOU is defined as the intersection area ratio of the segmentation result and the label image. The calculation results are summarized in Table 2. It can be seen from Table 2 that our model has satisfying classification and segmentation accuracy for defects. This provides high reliability for subsequent defect and atom number calculation.

Compared with manual methods, the applications of machine learning methods enable us to conduct statistical analysis of various defect data on a relatively large scale. Therefore, the point defect ratio and TM layer spacing are calculated to perform quantitative analysis as shown in Fig. 10. The point defect ratio is the ratio of defect numbers to all atoms in the STEM images. This ratio qualitatively represents the phase stability of the electrode materials.

**Table 1.** A confusion matrix for the defect prediction in testing datasets.

		Predicted				
		Li vacancy	TM vacancy	TM interstitial	Lattice atom	Background
Actual	Li vacancy	420	0	0	0	57
	TM vacancy	0	519	0	0	42
	TM interstitial	0	0	540	0	60
	Lattice atom	0	0	0	67536	708
	Background	51	78	69	1488	0

**Table 2.** Defects and atoms recognition results with four metrics.

Class	Precision (%)	Recall (%)	$F_1$ score (%)	IOU (%)
Li vacancy	89.17	88.05	88.61	80.83
TM vacancy	86.93	92.51	89.63	78.1
TM interstitial	88.67	90.00	89.33	70.65
Lattice atom	97.84	98.96	98.40	88.98

TM layer spacing is defined as the interplanar spacing in [001] direction. The distance between dense transition metal atomic layers along the *c* axis has a great impact on the number of lithium storage sites, which can roughly reflect the electrochemical capacity of NCM materials<sup>18,26,27</sup>. Detailed discussions of these two quantitative indicators will be carried out in the following parts.

NCM523 battery was cycled and aged to 5 different states. After discharge, the batteries were disassembled to obtain the electrode material for STEM analysis. The specific states of charge (SOC) are 100%, 90%, 70%, 30%, 10%, as shown in Fig. 10d. At the beginning of the cycle, NCM523 is all in the layered structure. Then spinel phase and rock-salt phase are gradually formed in turns. When the capacity decays to about 10%, it completely becomes the rock-salt phase. The point defect ratios in different SOC are 9, 24, 39, 73, and 48 per 1000 atoms, respectively. Traces of lithium vacancies occur first with little damage to the crystal structure. A small amount of transition metal vacancies come into existence later due to the strong oxidation of transition metals, which is related to the decomposition of electrolytes with a narrow electrochemical window<sup>2,3</sup>.

During the middle SOC, the spinel phase belongs to the transition phase, so there are a large number of point defects caused by phase transformation, and the defect ratio is the highest. The initial layered structure and the final rock-salt phase are relatively stable equilibrium phases, so the number of defects is less. The energy of the rock-salt phase after complete degradation is more stable and it has lost the ability to accommodate lithium ions<sup>14,28</sup>. More STEM images from different SOC are needed to determine the precise SOC value where the point defect ratio reaches its maximum. However, the rule that the number of point defects increases first and then decreases should be generally consistent with this observation.

The proposed u-net network can also be used to locate TM atoms through labeling the transition metal atom positions in the dataset, as shown in Fig. 9b. The total number of atoms in the picture can be quickly calculated by using border following algorithm<sup>29</sup>. The TM atom locating and counting results facilitate the statistical analysis of TM layer spacing. The layer spacing values in different SOC are proposed to be different during the aging process<sup>30</sup>. Hence, the TM layer spacing of MCM particles is investigated as shown in Fig. 10d. In the STEM images, each atom has two adjacent TM atoms along the *c* axis. The average of *c* axis coordinate differences with the two adjacent atoms is considered as the TM layer spacing label for this atom. Then over 45,000 TM atoms are sampled to calculate the mean value as the final TM

layer spacing for current SOC. The TM layer spacing decreases from 4.86 Å to 1.97 Å as capacity decays to 10% of the initial capacity (Fig. 10d). This highlights the importance of robust layered structure and appropriate layer spacing of single crystal NCM materials for longer battery cycle life. This also implies that expanding the layer spacing to restore more lithium storage sites in failure NCM materials might be one of the effective methods for battery capacity regeneration<sup>23,28</sup>.

Through the high-throughput deep learning of NCM electron microscopy data, this research classifies and counts the states, categories, and quantity of material crystal defects, explores the corresponding relationship between cycle life and microscopic crystal structures, and provides more profound insights into the aging mechanism and physical and chemical reaction of ternary layered cathode materials. Thus, the macro properties of battery materials can be better understood and controlled. This analysis is helpful to deeply understand the defect evolution and chemical transformation related to the degradation of layer cathode materials and to design battery materials with longer service life. The general machine learning data analysis framework can also greatly promote the theoretical development and technological progress of other materials science fields.

## METHODS

### Preparation of degraded NCM powders

NCM523 (Sigma-Aldrich) powders as cathode materials and graphite as anode materials were purchased to assemble pouch cells. PVDF (Aladdin) and super-P (SP, Aladdin) were used as binders and conductive additives, respectively. The graphite slurry with a weight ratio of graphite:binder:SP = 8:1:1 were coated on Cu foils as the anodes. The NCM slurry with a weight ratio of NCM523:binder:SP = 7:2:1 were coated on Al foils to form the cathodes. 1 M LiPF<sub>6</sub> solution was selected as the electrolyte, and the solvent was a mixture of vinyl carbonate (EC), dimethyl carbonate neutralization (DMC), and methyl ethyl carbonate (EMC) in a volume ratio of 1:1:1. The pouch cells were cycled at 1 C rate in the voltage range of 3.0 V to 4.2 V until the capacity retention rate is less than 10% of the original capacity. The cathode films were obtained by disassembling the pouch cells and wetting the cathode surfaces with a few drops of DMC solvent. This step is followed by drying the films in a vacuum oven at 70°C for 12 h to remove the residual electrolyte and lithium salts. The cathode materials were scraped from the aluminum foil and immersed in N-methyl-2-pyrrolidone solvent to remove the residual PVDF binders. Finally, the degraded NCM powders were obtained after centrifuging, drying, and screening the mixed solution.

### STEM experiment

Firstly, we grind the prepared NCM powder to below 500 nm, disperse the sample in absolute ethanol by ultrasonic dispersion, and finally pick it up with a support copper grid. Focused ion beam equipment was used to cut the NCM particles along the dislocation jogs to expose the interest crystallographic plane.



Atomic resolution STEM imaging was performed using JEM2100F/Titan G2 60–300 transmission electron microscope, which is equipped with a double spherical aberration corrector and operated at 60–300 kV. A low-dose beam shower was performed within 60 seconds before imaging to remove unstable organic impurities on the sample surfaces. The high-angle annular dark-field (HAADF) STEM images were acquired with a convergence angle of 31 mrad and a HAADF detector inner and outer collection angles of 86 and 200 mrad, respectively. The STEM images were introduced to the DL network without any post-processing.

## DATA AVAILABILITY

The raw images of NCM523 in our analysis process are available at <https://doi.org/10.5281/zenodo.5810209><sup>22</sup>.

## CODE AVAILABILITY

All the relevant code is available from the authors upon request.

Received: 21 January 2022; Accepted: 13 October 2022;

Published online: 03 November 2022

## REFERENCES

- Sun, C. et al. High-voltage cycling induced thermal vulnerability in LiCoO<sub>2</sub> cathode: cation loss and oxygen release driven by oxygen vacancy migration. *ACS Nano* **14**, 6181–6190 (2020).
- Wan, H. et al. Unraveling TM migration mechanisms in LiNi<sub>1/3</sub>Mn<sub>1/3</sub>Co<sub>1/3</sub>O<sub>2</sub> by modeling and experimental studies. *Nano Lett.* **21**, 6875–6881 (2021).
- Ko, D.-S. et al. Microstructural visualization of compositional changes induced by transition metal dissolution in Ni-rich layered cathode materials by high-resolution particle analysis. *Nano Energy* **56**, 434–442 (2019).
- Maleki Kheimeh Sari, H. & Li, X. Controllable cathode–electrolyte interface of Li[Ni<sub>0.8</sub>Co<sub>0.1</sub>Mn<sub>0.1</sub>]O<sub>2</sub> for lithium ion batteries: a review. *Adv. Energy Mater.* **9**, 1901597 (2019).
- Sun, H. H. et al. Beyond doping and coating: prospective strategies for stable high-capacity layered Ni-rich cathodes. *ACS Energy Lett.* **5**, 1136–1146 (2020).
- Zahrt, A. F. et al. Prediction of higher-selectivity catalysts by computer-driven workflow and machine learning. *Science* **363**, eaau5631 (2019).
- Lee, B. et al. Statistical characterization of the morphologies of nanoparticles through machine learning based electron microscopy image analysis. *ACS Nano* **14**, 17125–17133 (2020).
- Han, B. et al. Deep-learning-enabled fast optical identification and characterization of 2D materials. *Adv. Mater.* **32**, e2000953 (2020).
- Li, W., Field, K. G. & Morgan, D. Automated defect analysis in electron microscopic images. *npj Comput. Mater.* **4**, 36 (2018).
- Maksov, A. et al. Deep learning analysis of defect and phase evolution during electron beam-induced transformations in WS<sub>2</sub>. *npj Comput. Mater.* **5**, 12 (2019).
- Ziatdinov, M. et al. Quantifying the dynamics of protein self-organization using deep learning analysis of atomic force microscopy data. *Nano Lett.* **21**, 158–165 (2021).
- Ronneberger, O., Fischer, P. & Brox, T. U-Net: convolutional networks for biomedical image segmentation. *Lect. Notes Comput. Sci.* **9351**, 234–241 (2015).
- Wang, Q. et al. ECA-Net: Efficient Channel Attention for Deep Convolutional Neural Networks. *In: Proceedings Conference on Computer Vision and Pattern Recognition*, 11534–11542 (2020).
- Li, S. et al. Direct observation of defect-aided structural evolution in a nickel-rich layered cathode. *Angew. Chem. Int. Ed.* **59**, 22092–22099 (2020).
- Liu, S., Xiong, L. & He, C. Long cycle life lithium ion battery with lithium nickel cobalt manganese oxide (NCM) cathode. *J. Power Sources* **261**, 285–291 (2014).
- Zhan, C., Wu, T., Lu, J. & Amine, K. Dissolution, migration, and deposition of transition metal ions in Li-ion batteries exemplified by Mn-based cathodes – a critical review. *Energy Environ. Sci.* **11**, 243–257 (2018).
- Sun, H.-H. & Manthiram, A. Impact of microcrack generation and surface degradation on a nickel-rich layered Li[Ni<sub>0.9</sub>Co<sub>0.05</sub>Mn<sub>0.05</sub>]O<sub>2</sub> cathode for lithium-ion batteries. *Chem. Mater.* **29**, 8486–8493 (2017).
- Gong, Y. et al. In situ atomic-scale observation of electrochemical delithiation induced structure evolution of LiCoO<sub>2</sub> cathode in a working all-solid-state battery. *J. Am. Chem. Soc.* **139**, 4274–4277 (2017).
- Hjorth Larsen, A. et al. The atomic simulation environment—a Python library for working with atoms. *J. Phys. Condens Matter* **29**, 273002 (2017).
- Madsen, J. et al. A deep learning approach to identify local structures in atomic-resolution transmission electron microscopy images. *Adv. Theor. Simul.* **1**, 1800037 (2018).
- Madsen, J. & Susi, T. The abTEM code: transmission electron microscopy from first principles. *Open Res. Eur.* **1**, 13015 (2021).
- Cao, Y.-C. Scanning transmission electron microscopy data of LiNi<sub>0.5</sub>Co<sub>0.2</sub>Mn<sub>0.3</sub>O<sub>2</sub> single crystal Cathode materials during degradation process [Data set]. *Zenodo* <https://doi.org/10.5281/zenodo.5810209> (2021).
- Guo, Y. et al. High reversibility of layered oxide cathode enabled by direct Re-generation. *Energy Storage Mater.* **43**, 348–357 (2021).
- Wen, B. et al. Ultrafast ion transport at a cathode–electrolyte interface and its strong dependence on salt solvation. *Nat. Energy* **5**, 578–586 (2020).
- Li, Z. et al. Engineering oxygen vacancies in a polysulfide-blocking layer with enhanced catalytic ability. *Adv. Mater.* **32**, e1907444 (2020).
- Liu, W. et al. Nickel-rich layered lithium transition-metal oxide for high-energy lithium-ion batteries. *Angew. Chem. Int. Ed.* **54**, 4440–4458 (2015).
- Jung, S.-K. et al. Understanding the degradation mechanisms of LiNi<sub>0.5</sub>Co<sub>0.2</sub>Mn<sub>0.3</sub>O<sub>2</sub> cathode material in lithium ion batteries. *Adv. Energy Mater.* **4**, 1300787 (2014).
- Chen, M. et al. Recycling end-of-life electric vehicle lithium-ion. *Batteries. Joule* **3**, 2622–2646 (2019).
- Satoshi, Suzuki et al. Topological structural analysis of digitized binary images by border following. *Comput. Vision Graphics Image Proc.* **30**, 32–46 (1985).
- Zuo, W. et al. Engineering Na(+)-layer spacings to stabilize Mn-based layered cathodes for sodium-ion batteries. *Nat. Commun.* **12**, 4903 (2021).

## ACKNOWLEDGEMENTS

This project was supported by the fund from National Natural Science Foundation of China (NSFC No. 52077096 and 52107224), China Postdoctoral Science Foundation under Grant No. 2019M662612, the Interdisciplinary Program of Wuhan National High Magnetic Field Center from Huazhong University of Science and Technology (Grant No. WHMFC202138) and State Grid Zhejiang Electric Power Co., Ltd. technology project 5211UZ2000K1.

## AUTHOR CONTRIBUTIONS

Y.-C.C. and S.L. conceived the idea. Y.G. synthesized materials and acquired the STEM data. W.S. and D.C. wrote the code, analyzed the data, and wrote the paper. Y.G. and Q.H. aided in the interpretation of the results. W.S. and Y.G. were co-first authors and contributed equally to this work. All authors commented on the manuscript.

## COMPETING INTERESTS

The authors declare no competing interests.

## ADDITIONAL INFORMATION

**Supplementary information** The online version contains supplementary material available at <https://doi.org/10.1038/s41524-022-00905-5>.

**Correspondence** and requests for materials should be addressed to Yuan-Cheng Cao.

**Reprints and permission information** is available at <http://www.nature.com/reprints>

**Publisher's note** Springer Nature remains neutral with regard to jurisdictional claims in published maps and institutional affiliations.



**Open Access** This article is licensed under a Creative Commons Attribution 4.0 International License, which permits use, sharing, adaptation, distribution and reproduction in any medium or format, as long as you give appropriate credit to the original author(s) and the source, provide a link to the Creative Commons license, and indicate if changes were made. The images or other third party material in this article are included in the article's Creative Commons license, unless indicated otherwise in a credit line to the material. If material is not included in the article's Creative Commons license and your intended use is not permitted by statutory regulation or exceeds the permitted use, you will need to obtain permission directly from the copyright holder. To view a copy of this license, visit <http://creativecommons.org/licenses/by/4.0/>.

© The Author(s) 2022